Tailoring optoelectronic performance through compositional engineering to optimize trap densities in $Cs_xMA_{(1-x)}PbI_3$ perovskite nanowires

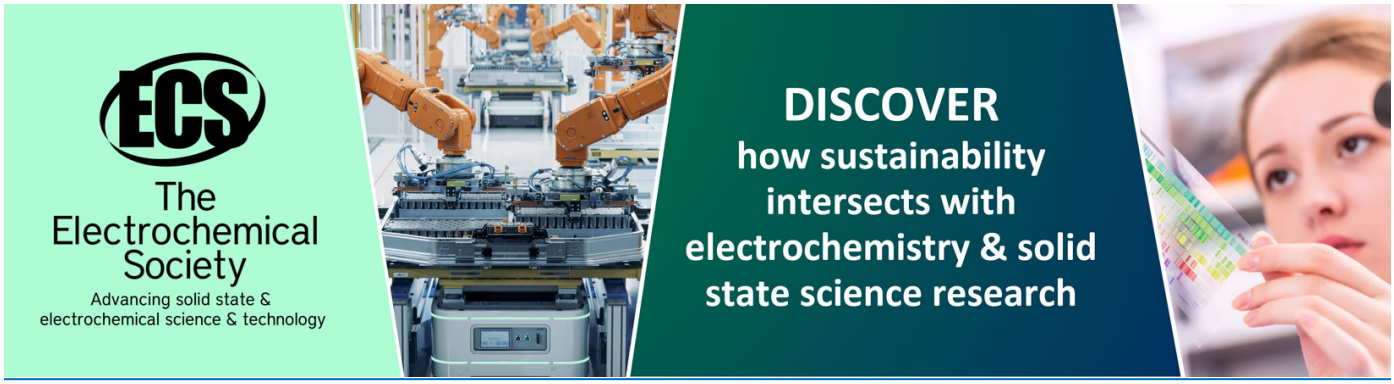

OPEN ACCESS
IOP Publishing
Journal of Physics D: Applied Physics
J. Phys. D: Appl. Phys. **57** (2024) 215101 (8pp)
https://doi.org/10.1088/1361-6463/ad2a13

Tailoring optoelectronic performance through compositional engineering to optimize trap densities in $Cs_xMA_{(1-x)}PbI_3$ perovskite nanowires

Bin Han[1,*], Yu Hu[1,2], Bo Liu[1,2], Guanghui Wang[1,2], Qi Qiu[1,2], Yanren Tang[1,2], Shufang Ma[1], Bingshe Xu[1,3,4], Bocang Qiu[1,*] and Hsien-Yi Hsu[5,6,*]

[1] Materials Institute of Atomic and Molecular Science, Shaanxi University of Science and Technology, Xi'an, Shaanxi 710021, People's Republic of China
[2] School of Materials Science and Engineering, Shaanxi University of Science and Technology, Xi'an, Shaanxi 710021, People's Republic of China
[3] Key Laboratory of Interface Science and Engineering in Advanced Materials, Taiyuan University of Technology, Taiyuan 030024, People's Republic of China
[4] Shanxi-Zheda Institute of Advanced Materials and Chemical Engineering, Taiyuan 030024, People's Republic of China
[5] School of Energy and Environment and Department of Materials Science and Engineering, City University of Hong Kong, Kowloon Tong, Hong Kong Special Administrative Region of China, People's Republic of China
[6] Shenzhen Research Institute of City University of Hong Kong, Shenzhen 518057, People's Republic of China

E-mail: binhan@sust.edu.cn, qiubc@lumcore.com and sam.hyhsu@cityu.edu.hk

Received 14 November 2023, revised 26 January 2024
Accepted for publication 16 February 2024
Published 26 February 2024

Abstract

Organic-inorganic methylammonium lead iodide perovskite ($MAPbI_3$) nanowires (NWs) have attracted significant attention in the realm of optoelectronic devices due to their outstanding optoelectronic properties. However, the persistent challenge of high trap densities has been a limiting factor in realizing their full potential in device performance. To address this challenge, we incorporated cesium (Cs) and systematically investigated the impact of Cs concentration on the trap densities and the optoelectronic characteristics of $Cs_xMA_{(1-x)}PbI_3$ NWs. Our findings unveiled an initial reduction in trap densities as Cs^+ content increased, with the lowest point occurring at $x = 0.2$. However, beyond this threshold, trap densities began to rise, eventually surpassing those observed in pure $MAPbI_3$ at $x = 0.4$. Furthermore, we fabricated single NW photodetectors to assess how Cs^+ content influenced optoelectronic properties. The results indicated that Cs^+ incorporation led to enhancements in photocurrent and response speed, with

* Authors to whom any correspondence should be addressed.

the optimal performance observed at $x = 0.2$. Our study provides valuable insights into the role of Cs^+ incorporation in tailoring the optoelectronic properties of perovskite NWs.

Supplementary material for this article is available online

Keywords: organic-inorganic hybrid perovskites, nanowires, Cs^+ incorporation, trap density, optoelectronic properties

1. Introduction

One-dimensional semiconductor nanowires (NWs) exhibit unique geometries and properties, establishing them as promising foundational elements in a range of nanoscale electronic and optoelectronic devices, including photodetectors, transistors, memory devices, photovoltaics, and nanogenerator [1–6]. Among the emerging materials in the realm of diverse optoelectronic devices, organic-inorganic lead halide perovskites, particularly methylammonium lead halide perovskite ($MAPbX_3$, where X = Cl, Br, I), stand out due to their exceptional attributes, including an ultrahigh absorption coefficient, tunable band gap, high carrier mobility, and cost-effective fabrication [7–12]. Notably, $MAPbI_3$, a representative member of the $MAPbX_3$ family, boasts exceptional light-harvesting capabilities with an absorption coefficient as high as 10^5 cm^{-1}, surpassing existing optoelectronic materials [13]. Consequently, $MAPbI_3$ NWs have found applications in high-performance optoelectronic devices such as photodetectors [14, 15], light-emitting diodes [9], and lasers [16, 17]. For example, $MAPbI_3$ NW-based photodetectors have exhibited remarkable characteristics, including low dark current ($\leqslant$1 nA) [18] and high detectivity ($\geqslant 10^{12}$ Jones) [19]. However, despite their excellent optoelectronic properties, the presence of a high trap densities remains a significant impediment to further enhancing device performance.

The elevated trap densities exacerbate the capture and recombination of photogenerated carriers, leading to diminished photocurrent and slower response speeds in devices [20, 21]. Consequently, there is an urgent imperative to develop a straightforward yet effective method for reducing trap densities in $MAPbI_3$ NWs. Several strategies have been proposed to mitigate trap densities in organic halide perovskites, and among these, the creation of mixed cation perovskites has emerged as a successful approach to reduce trap densities and optimize optoelectronic properties [22–24]. One effective method involves introducing larger organic cations like formamidinium (FA^+) in place of some of the methylammonium (MA^+), thereby enhancing the optoelectronic characteristics of perovskites [19, 25–27]. Additionally, it has been demonstrated that the partial substitution of MA^+ with small inorganic cations such as cesium cation (Cs^+) can alter the interaction between $[PbI_6]^+$ and I^-, leading to crystal lattice shrinkage, reduced atomic vacancies, lower trap densities, and improved optoelectronic properties [28–30]. Despite the booming strategies and developments in constructing various mixed cation perovskites, our understanding of the optimal concentration of Cs^+ in $MAPbI_3$ NWs for achieving the best photoelectric properties remains limited. In other words, it remains unclear whether there exists an optimum Cs^+ concentration in $MAPbI_3$ NWs to yield the most favorable optoelectronic characteristics. Thus, there is an urgent need to elucidate how varying concentrations of Cs^+ impact trap densities and optoelectronic properties.

In this study, we conducted a systematic exploration of the impact of Cs^+ concentration on both the trap densities and the optoelectronic properties of $MAPbI_3$ perovskite NWs. Our investigation revealed that Cs^+ incorporation yielded a substantial reduction in trap densities, accompanied by significant improvements in optoelectronic properties. However, it is noteworthy that an excessive amount of Cs^+ incorporation led to the increase in trap densities, consequently leading to a degradation in device performance.

2. Experimental section

2.1. Preparation of $Cs_xMA_{(1-x)}PbI_3$ NWs

To prepare $Cs_xMA_{(1-x)}PbI_3$ NWs, we first created a precursor solution with a concentration of 0.04 M. This solution was formulated by dissolving CsI, MAI, and PbI_2 in a molar ratio of x:(1−x):1 (x = 0, 0.1, 0.2, 0.3, 0.4, 0.6 and 0.8), all within 2.5 ml of dimethylformamide (DMF). Then, a drop of the precursor was dropped on a clean Si/SiO_2 substrate placed on a holder in a container with isopropyl alcohol (IPA) injected in it. Afterward, the container was sealed and heated by a hot plate at 90 °C for 60 min to form the intermediate phase NWs. Finally, the intermediate phase NWs were heated at 100 °C for 20 min to transfer to the α phase NWs.

2.2. Characterization of $Cs_xMA_{(1-x)}PbI_3$ NWs

Scanning electron microscope (SEM) and energy-dispersive spectroscopy (EDS) results of the NWs were measured using a JEOL JIB-4700F with an accelerating voltage of 10 kV. X-ray diffraction (XRD) was measured using a Bruker D8 diffractometer with monochromatic Cu Kα radiation (λ = 1.5406 Å). Absorbance was measured using an ultraviolet-visible (UV–Vis) spectrophotometer (Agilent cary 5000), and photoluminescence (PL) spectra were measured using a 532 nm laser (Horiba Scientific).

2.3. Device fabrication and characterization

The single NW photodetectors were prepared by deposition of 50 nm thick Au through a shadow mask. The photoelectric properties of the photodetector and space-charge-limited-current (SCLC) technique were carried out at room temperature by using a semiconductor parameter analyzer (Keithley 4200A-SCS) combined with a probe station. The response speed of the devices was measured using a digital oscilloscope (Keysight DSOX1102G) coupled with a low-noise current preamplifier (Stanford Research System SR570).

3. Results and discussion

We employed a straightforward and time-efficient low-temperature solution-based method, as previously detailed in our publication, to grow $Cs_xMA_{(1-x)}PbI_3$ NWs [15]. In brief, a precursor solution with a predetermined Cs/MA ratio was deposited onto a Si/SiO_2 substrate and subsequently subjected to heating to facilitate the formation of perovskite NWs. A comprehensive description of the NWs growth process is provided in the experimental section. For the investigation into the influence of Cs^+ concentration on the properties of the perovskite NWs, we prepared NWs with Cs/MA ratios ranging from $x = 0 - 0.4$. Figure 1 presents SEM images of the $Cs_xMA_{(1-x)}PbI_3$ NWs. Across all samples, the NWs display lengths spanning several micrometers. Within the insets of individual NW SEM images, we observed that the diameter of pure $MAPbI_3$ NWs is approximately 900 nm. Conversely, in the mixed cation $Cs_xMA_{(1-x)}PbI_3$ samples, the diameter reduces to around 600 nm due to the lattice shrinkage induced by Cs^+ [29, 30]. Furthermore, obvious agglomerates are observed in samples with $x = 0.3$ and 0.4, marked by yellow frames. An enlarged SEM image (figure 1(f)) offers evidence that these agglomerates consist of short NWs. To scrutinize the composition of these NWs, we conducted an EDS analysis, the results of which are presented in table 1. The I:Pb ratio obtained from EDS smaller than 3:1 is mainly due to the unstable nature of the organic perovskite [18, 31]. From the EDS mapping results (figure S1), it can be observed that all the elements are distributed homogeneously. It is evident that the Cs^+ concentrations closely align with the intended molar concentrations in the precursors in the $Cs_{0.1}MA_{0.9}PbI_3$ and $Cs_{0.2}MA_{0.8}PbI_3$ samples. However, in samples with higher x values of 0.3 and 0.4, the Cs^+ concentration falls below the designed amount, attributed to the formation of $CsPbI_3$ NWs, which consumes Cs^+ from the precursors. Additionally, the composition of the short NWs within the agglomerates is primarily $CsPbI_3$. Similar results are also observed in the $x = 0.6$ and 0.8 samples as shown in figure S2.

To explore the impact of chemical composition on the structure of perovskite NWs, we performed XRD analysis on $Cs_xMA_{(1-x)}PbI_3$ NWs, with the results depicted in figure 2. Samples without Cs^+ or with low Cs^+ concentrations ($x = 0$, 0.1, 0.2) exhibit distinct diffraction peaks associated with the α-phase perovskite. In contrast, samples with higher Cs^+ content ($x = 0.3$ and 0.4) reveal additional characteristic diffraction peaks corresponding to the δ-phase $CsPbI_3$ (figure 2(a)). This observation aligns with the SEM findings, confirming the presence of short NWs composed of $CsPbI_3$ in samples with elevated Cs^+ content. Furthermore, upon closer examination of the (110) plane within the 13.6°–14.8° range in figure 2(b), it becomes evident that the diffraction angle gradually shifts toward higher angles with increasing Cs^+ content. This shift suggests a reduction in the lattice parameters, consistent with the Bragg equation: $2d\sin\theta = n\lambda$. The incorporation of Cs^+ is thus responsible for lattice shrinkage, attributed to the smaller size of Cs^+ compared to MA^+. The Goldschmidt tolerance factors ($t_{effective}$) for the $Cs_xMA_{1-x}PbI_3$ nanowires are calculated by the following formula [32]:

$$r_{\text{effective}} = x r_{Cs^+} + (1-x)\, r_{MA^+}$$

$$t_{\text{effective}} = \frac{r_{\text{effectivc}} + r_{I^-}}{\sqrt{2}\,(r_{Pb^{2+}} + r_{I^-})}$$

where $r_{\text{effective}}$ is the effective A-site ionic radius, x and $(1-x)$ is the molar ratio of Cs^+ to MA^+, and r_{Cs^+}, r_{MA^+}, $r_{Pb^{2+}}$, r_{I^-} are the ionic radii of Cs, MA, Pb, and I elements, respectively. The calculated tolerance factors are 0.912, 0.905, 0.901, 0.897 and 0.894 for the $x = 0$, 0.1, 0.2, 0.3, and 0.4 samples, respectively. To show the crystalline quality of the nanowires, we extracted the full-width at half-maximum (FWHM) of the (110) peaks from the XRD results. It can be observed that the FWHM decreases first and then increases. When $x = 0.2$, the FWHM is the smallest and the crystal quality is the highest. FWHM increases when the x value exceeding 0.2, indicating that the crystal quality decreased. Similar findings have been reported in the case of Cs-doped $MAPbBr_3$ single crystals [29].

The incorporation of Cs^+ also has a significant impact on the optical properties of the mixed-cation perovskite. In figure 3(a), we observe the UV–Vis absorption spectra of $Cs_xMA_{(1-x)}PbI_3$ NWs. Notably, these spectra reveal a consistent blue shift in the absorption edges as the value of x increases, indicating that Cs^+ incorporation leads to a widening of the bandgap. This shift is further confirmed by the corresponding bandgap values extracted from the $(\alpha h\nu)^2$-$(h\nu)$ curve (figure 3(b)), which demonstrate an increase from 1.54 eV to 1.61 eV with the ascending Cs^+ content. A similar blue shift, attributed to the presence of Cs^+, is also evident in the normalized PL spectra, as depicted in the inset of figure 3(c), in agreement with the UV–Vis observations. It is worth noting that the PL intensities of $Cs_xMA_{(1-x)}PbI_3$ NWs exhibit a consistent increase as Cs^+ concentrations rise from $x = 0 - 0.2$ (figure 3(c)). However, these PL intensities steadily decrease as the x value surpasses 0.2 and reaches 0.4. This observed trend is similar to the patterns observed in the XRD intensities. The reduction in PL intensities is believed to be associated with the increased trap densities resulting from the excessive incorporation of Cs^+ [33, 34].

To assess the trap densities within $Cs_xMA_{(1-x)}PbI_3$ NWs, we conducted SCLC measurements in a dark environment

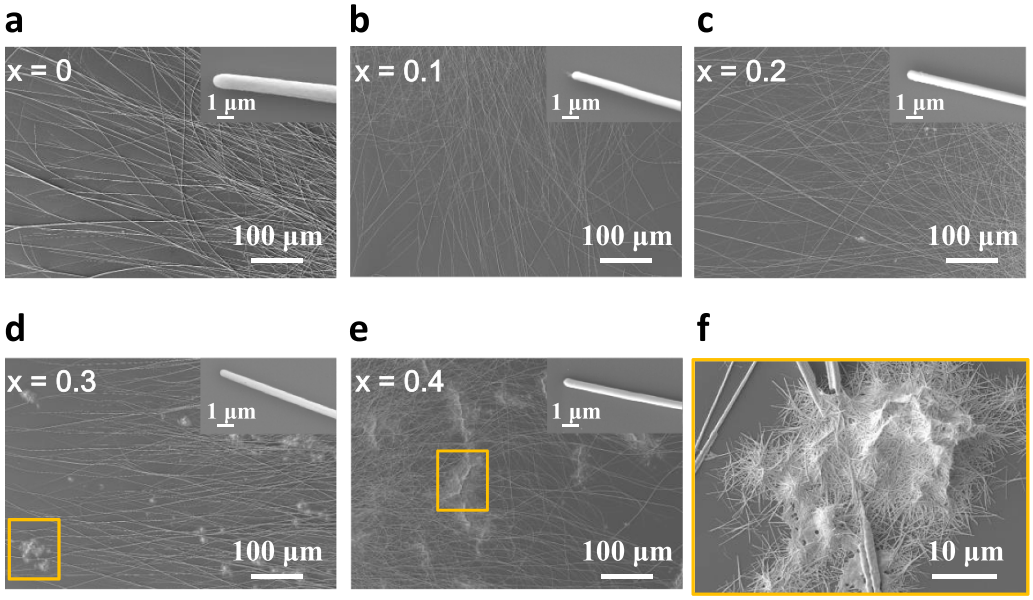

Figure 1. (a)–(e) SEM images of $Cs_xMA_{(1-x)}PbI_3$ NWs with x value ranging from 0 to 0.4, the insets are the enlarged individual NWs. (f) The enlarged NWs marked by yellow frames in (d) and (e).

Table 1. Element content proportion by EDS from the synthesized $Cs_xMA_{(1-x)}PbI_3$ NWs.

	EDS measured results of NWs (%)				
Molecule formula	Cs	N	Pb	I	Ratio
$X = 0$	0	14.56 ± 4.20	15.65 ± 1.96	46.03 ± 5.61	0.00: 0.94: 1: 2.94
$X = 0.1$	1.78 ± 0.40	13.62 ± 2.55	16.63 ± 1.41	47.10 ± 3.56	0.11: 0.82: 1: 2.83
$X = 0.2$	3.03 ± 0.59	12.54 ± 1.92	16.24 ± 1.47	45.68 ± 3.87	0.19: 0.77: 1: 2.81
$X = 0.3$	3.90 ± 0.64	11.99 ± 1.66	16.07 ± 1.00	45.20 ± 2.98	0.24: 0.74: 1: 2.81
$X = 0.4$	4.73 ± 1.20	11.38 ± 1.98	15.88 ± 1.16	44.85 ± 2.92	0.29: 0.71: 1: 2.82

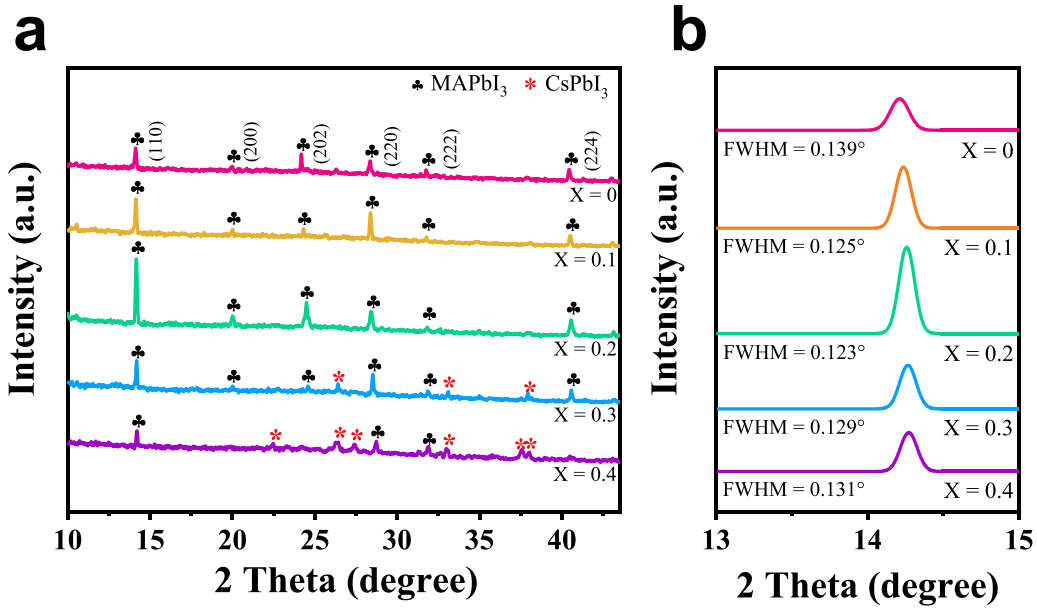

Figure 2. The XRD patterns (a) and the local enlarged XRD patterns (b) of $Cs_xMA_{(1-x)}PbI_3$ NWs.

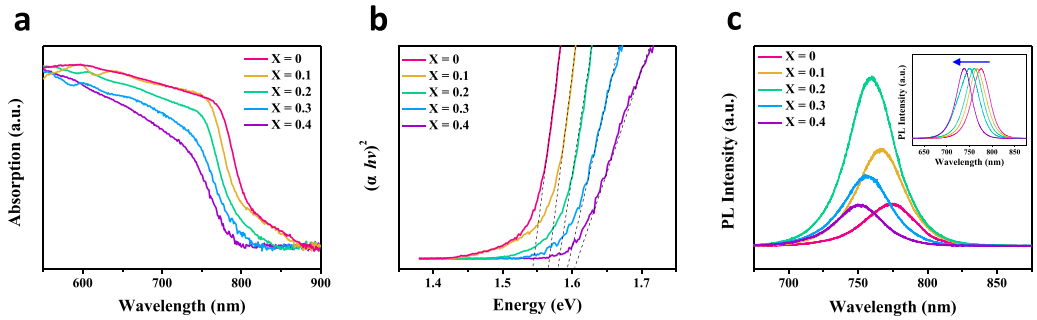

Figure 3. Characterizations of optical properties of $Cs_xMA_{(1-x)}PbI_3$ NWs: (a) UV–Vis absorption spectra, (b) band gaps, and (c) PL spectra (inset is the normalized PL spectra).

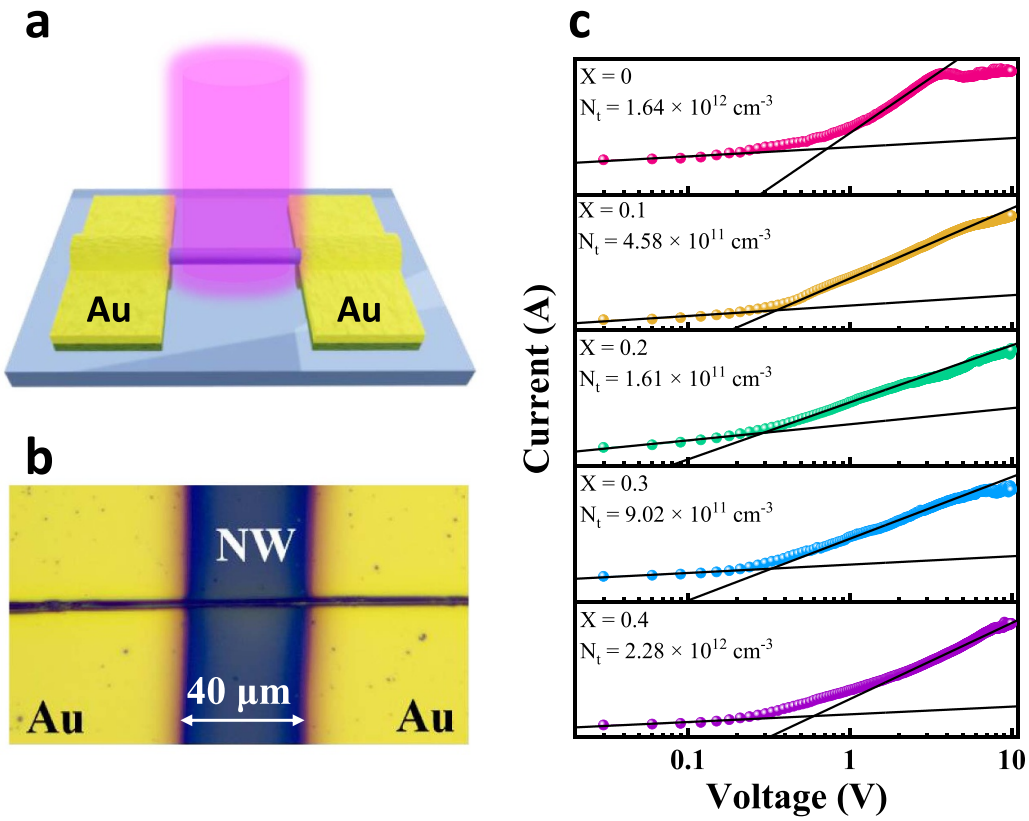

Figure 4. The schematic (a) and the optic image (b) of the single NW device. (c) *I–V* responses of $Cs_xMA_{(1-x)}PbI_3$ NWs devices measured in dark.

using single NW devices for all the samples with similar diameter, as depicted in figures 4(a) and (b). As illustrated in figure 4(c), the current-voltage (*I–V*) response exhibited a linear behavior at lower voltages, followed by a rapid nonlinear increase as it entered the regime known as the trap-filled limit (TFL), characterized by the onset voltage V_{TFL}. In this TFL region, all available trap states were saturated with injected carriers. Assuming the trap density is dominated by the volume trap states, the V_{TFL} value serves as the basis for calculating the trap densities through the following equation [35]:

$$V_{\mathrm{TFL}} = \frac{eN_t l^2}{2\varepsilon\varepsilon_0}$$

where N_t is the trap densities, l is the length of the NW, e is the elementary charge, ε is the dielectric constant of perovskites, and ε_0 is the vacuum permittivity. It is known that the current-voltage hysteresis in the organic perovskite is a common phenomenon due to the fast ion migration. To minimize the impact of hysteresis on the properties during the measurement, we performed a single *I–V* sweep with fast sweeping rate to obtain the *I–V* curves for all the samples. As depicted in figure 4(c), the trap densities within $Cs_xMA_{(1-x)}PbI_3$ NWs demonstrates an initial decline with increasing Cs^+ content, reaching its minimum value of 4.58×10^{11} cm^{-3} at $x = 0.2$. However, as Cs^+ content continues to rise, the trap densities begin to increase. Remarkably, in the $x = 0.4$, 0.6

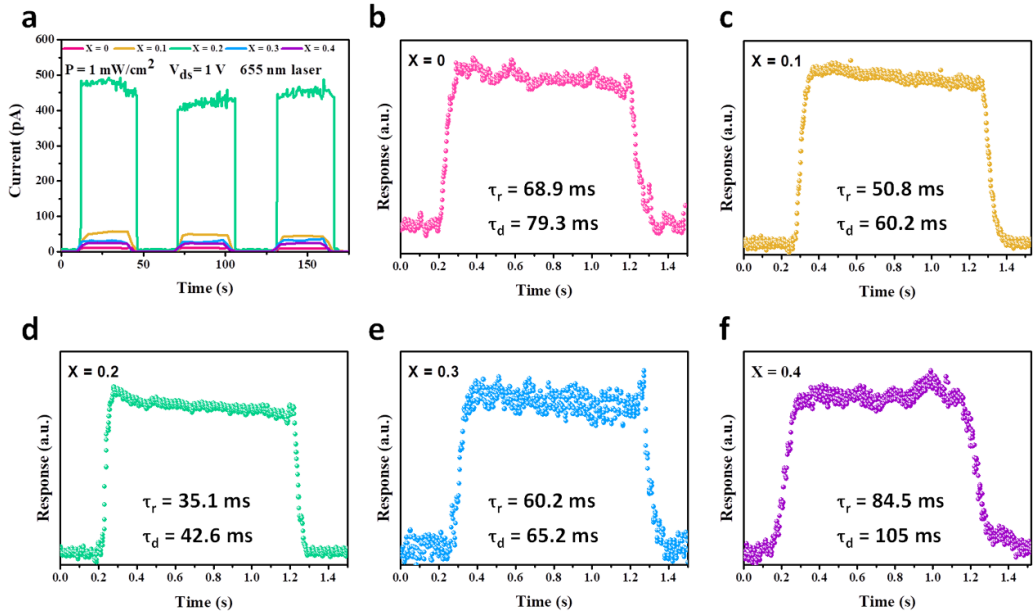

Figure 5. (a) Photoswitching characteristics of the $Cs_xMA_{(1-x)}PbI_3$ NW photodetectors measured at 1 V under 655 nm unfocused laser with light intensity of 1 mW cm^{-2}. (b)–(f) The response speed of the $Cs_xMA_{(1-x)}PbI_3$ NW photodetectors.

and 0.8 samples (figure S2), the trap densities surpasse that of pure $MAPbI_3$, signifying that excessive Cs^+ leads to an elevation in trap states. To estimate the effect of surface trap states, we passivated the nanowires by deposition of SiO_2 on the devices. It is found that the trap density decreased slight after SiO_2 passivation (figure S3), which indicated that the surface trap density is relatively small compared with the volume trap density. These findings, derived from the SCLC analysis, align consistently with the results obtained from XRD and PL measurements, thus confirming that $Cs_{0.2}MA_{0.8}PbI_3$ NWs exhibit both high crystal quality and PL intensity. The notably low trap densities offer substantial advantages by reducing the recombination and release of photogenerated carriers. This characteristic proves particularly beneficial for enhancing the optoelectronic properties of perovskite devices.

To gain deeper insights into the influence of Cs^+ content on the optoelectronic properties of perovskite devices, we conducted a further analysis of single NW photodetectors (figure 5). The dynamic current-time photoresponses of $Cs_xMA_{(1-x)}PbI_3$ NWs photodetectors were recorded at 1 V under an incident light intensity of 1 mW cm^{-2} from a 655 nm unfocused laser, as depicted in figure 5(a). It is clearly observable that the inclusion of Cs^+ in the perovskite NWs leads to a substantial increase in photocurrent compared to NWs without Cs^+ incorporation. As the Cs^+ content varies, the photocurrent initially rises but subsequently declines. The maximum photocurrent, reaching 480 pA, is achieved within the $x = 0.2$ sample. Remarkably, the on/off ratio for the $Cs_{0.2}MA_{0.8}PbI_3$ NW photodetector is almost 48 times higher than that of pure $MAPbI_3$ NW. Moreover, alongside the enhanced photocurrent, the device's response speed also improves with Cs^+ incorporation. Figures 5(b)–(f) illustrate the response speed of the $Cs_xMA_{(1-x)}PbI_3$ NW photodetectors. Response speed encompasses both the rise and decay times (τ_r and τ_d), defined as the time taken for the photocurrent to increase from 10% to 90% of its peak value and vice versa [36]. Notably, the response speed of the $x = 0.1$, 0.2, and 0.3 $Cs_xMA_{(1-x)}PbI_3$ NW photodetectors surpasses that of pure $MAPbI_3$ NW, with the $Cs_{0.2}MA_{0.8}PbI_3$ photodetector exhibiting the swiftest rise and decay times. This emphasizes that Cs^+ incorporation effectively enhances the response speed. However, it is essential to note that the response speed of the $Cs_{0.4}MA_{0.6}PbI_3$ photodetector becomes slower than that of pure $MAPbI_3$. This indicates that excessive Cs^+ incorporation hinders the response speed. This phenomenon arises because excessive Cs^+ incorporation augments the trap densities within the perovskite, subsequently prolonging carrier release and recombination times [20]. It should be noted that the response speed of the nanowire devices is slower than that of their thin film and bulk counterparts. This is mainly due to the large surface-to-volume ratio and reduced screening, impurities and defects possibly act as trap centers in nanowires, which prolongs the carrier lifetime [37]. Moreover, to understand the efficiency of the photo conversion in these devices, we calculated the quantum efficiency (EQE) of different x value devices, as shown in figure S4. It was observed that the incorporation of Cs^+ in perovskite NWs resulted in a significant increase in EQE compared to NWs without Cs^+ incorporation. With the change of Cs^+ content, EQE first increased and then decreased, and the ability to convert optical signals into electrical signals was strongest at $x = 0.2$.

4. Conclusion

In summary, this study focused on the systematic investigation of the impact of Cs^+ incorporation on the trap densities and the optoelectronic properties of $Cs_xMA_{(1-x)}PbI_3$ mixed cation perovskite NWs. It was found that Cs^+ incorporation led to significant trap densities reduction. However, excessive Cs^+ incorporation resulted in an increase in trap densities. The reduction in trap densities, as observed in $Cs_{0.2}MA_{0.8}PbI_3$ NWs, was associated with improved crystal quality and photoluminescence intensity. These findings were further supported by SCLC measurements, demonstrating that $Cs_{0.2}MA_{0.8}PbI_3$ NWs exhibited the lowest trap densities among the studied compositions. In terms of optoelectronic performance, $Cs_{0.2}MA_{0.8}PbI_3$ NW-based photodetectors displayed significantly enhanced photocurrents and response speeds compared to pure $MAPbI_3$. However, it is crucial to note that excessive Cs^+ incorporation, as seen in $Cs_{0.4}MA_{0.6}PbI_3$, negatively impacted response speed due to increased trap densities. This work sheds light on the intricate relationship between Cs^+ incorporation and the properties of mixed cation perovskite NWs, providing valuable insights into optimizing the optoelectronic performance of these materials.

Data availability statement

All data that support the findings of this study are included within the article (and any supplementary files).

Acknowledgments

This work was financially supported in part by the National Natural Science Foundation of China (Grant No. 51901119), Scheme of the Shaanxi Province Qin-Chuang-Yuan Project (Grant No. 2023KXJ-188), Innovation and Technology Commission (Grant No. MHP/104/21), Shenzhen Science Technology and Innovation Commission (Grant Nos. JCYJ20210324125612035, R-IND12303 and R-IND12304), and City University of Hong Kong (Grant No. 9360140).

ORCID iDs

Bin Han https://orcid.org/0000-0001-6618-3194
Shufang Ma https://orcid.org/0000-0002-6689-6300

References

[1] Ram M S, Persson K-M, Irish A, Jönsson A, Timm R and Wernersson L-E 2021 High-density logic-in-memory devices using vertical indium arsenide nanowires on silicon *Nat. Electron.* **4** 914–20
[2] Balaghi L *et al* 2021 High electron mobility in strained GaAs nanowires *Nat. Commun.* **12** 6642
[3] Li D, Lan C, Manikandan A, Yip S, Zhou Z, Liang X, Shu L, Chueh Y-L, Han N and Ho J C 2019 Ultra-fast photodetectors based on high-mobility indium gallium antimonide nanowires *Nat. Commun.* **10** 1664
[4] Priolo F, Gregorkiewicz T, Galli M and Krauss T F 2014 Silicon nanostructures for photonics and photovoltaics *Nat. Nanotechnol.* **9** 19–32
[5] Han B, Shimizu Y, Wipakorn J, Nishibe K, Tu Y, Inoue K, Fukata N and Nagai Y 2016 Boron distributions in individual core–shell Ge/Si and Si/Ge heterostructured nanowires *Nanoscale* **8** 19811–5
[6] Wang Z L and Song J 2006 Piezoelectric nanogenerators based on zinc oxide nanowire arrays *Science* **312** 242–6
[7] Hsu H-Y, Ji L, Ahn H S, Zhao J, Yu E T and Bard A J 2015 A liquid junction photoelectrochemical solar cell based on p-type $MeNH_3PbI_3$ perovskite with 1.05 V open-circuit photovoltage *J. Am. Chem. Soc.* **137** 14758–64
[8] Lin R *et al* 2022 All-perovskite tandem solar cells with improved grain surface passivation *Nature* **603** 73–78
[9] Mak C H, Huang X, Liu R, Tang Y, Han X, Ji L, Zou X, Zou G and Hsu H-Y 2020 Recent progress in surface modification and interfacial engineering for high-performance perovskite light-emitting diodes *Nano Energy* **73** 104752
[10] Gao H, Feng J, Pi Y, Zhou Z, Zhang B, Wu Y, Wang X, Jiang X and Jiang L 2018 Bandgap engineering of single-crystalline perovskite arrays for high-performance photodetectors *Adv. Funct. Mater.* **28** 1804349
[11] Feng J, Mak C H, Yu L, Han B, Shen H H, Santoso S P, Yuan M, Li F F, Song H and Colmenares J C 2024 Structural modification strategies, interfacial charge-carrier dynamics, and solar energy conversion applications of organic–inorganic halide perovskite photocatalysts *Small Methods* **8** 2300429
[12] Han B, Liu B, Wang G, Qiu Q, Wang Z, Xi Y, Cui Y, Ma S, Xu B and Hsu H Y 2023 Transparent and reusable nanostencil lithography for organic–inorganic hybrid perovskite nanodevices *Adv. Funct. Mater.* **33** 2300570
[13] Green M A, Ho-Baillie A and Snaith H J 2014 The emergence of perovskite solar cells *Nat. Photon.* **8** 506–14
[14] Han B *et al* 2023 High-performance hybrid graphene-perovskite photodetector based on organic nano carbon source-induced graphene interdigital electrode film on quartz substrate *Carbon* **204** 547–54
[15] Wang G *et al* 2022 Mixed-dimensional van der Waals heterostructure for high-performance and air-stable perovskite nanowire photodetectors *ACS Appl. Mater. Interfaces* **14** 55183–91
[16] Zhang Q, Su R, Du W, Liu X, Zhao L, Ha S T and Xiong Q 2017 Advances in small perovskite-based lasers *Small Methods* **1** 1700163
[17] Zhu H, Fu Y, Meng F, Wu X, Gong Z, Ding Q, Gustafsson M V, Trinh M T, Jin S and Zhu X Y 2015 Lead halide perovskite nanowire lasers with low lasing thresholds and high quality factors *Nat. Mater.* **14** 636–42
[18] Dong D, Deng H, Hu C, Song H, Qiao K, Yang X, Zhang J, Cai F, Tang J and Song H 2017 Bandgap tunable $Cs_x(CH_3NH_3)_{1-x}PbI_3$ perovskite nanowires by aqueous solution synthesis for optoelectronic devices *Nanoscale* **9** 1567–74
[19] Wang H, Liu P, Zhang M, Han B, Wang G, Zhang J, Hu S, Li H, Guo Y and Zhao G 2023 Spraying perovskite intermediate enabling inch-scale microwire film fabrication for integration compatible efficient-photodetectors array *Adv. Funct. Mater.* **33** 2209942
[20] Hsiao Y-W, Song J-Y, Wu H-T, Hong K-T, Leu C-C and Shih C-F 2021 Effects of cesium content on the triple-cation lead halide perovskite photodetectors with enhanced detectivity and response time *J. Alloys Compd.* **889** 161621
[21] Xu X, Zhang X, Deng W, Huang L, Wang W, Jie J and Zhang X 2018 Saturated vapor-assisted growth of single-crystalline organic–inorganic hybrid perovskite

nanowires for high-performance photodetectors with robust stability *ACS Appl. Mater. Interfaces* **10** 10287–95
[22] Saidaminov M I *et al* 2018 Suppression of atomic vacancies via incorporation of isovalent small ions to increase the stability of halide perovskite solar cells in ambient air *Nat. Energy* **3** 648–54
[23] Shi Z, Zhang Y, Cui C, Li B, Zhou W, Ning Z and Mi Q 2017 Symmetrization of the crystal lattice of $MAPbI_3$ boosts the performance and stability of metal–perovskite photodiodes *Adv. Mater.* **29** 1701656
[24] Lee J W, Kim D H, Kim H S, Seo S W, Cho S M and Park N G 2015 Formamidinium and cesium hybridization for photo-and moisture-stable perovskite solar cell *Adv. Energy Mater.* **5** 1501310
[25] Bai D, Zhang J, Jin Z, Bian H, Wang K, Wang H, Liang L, Wang Q and Liu S F 2018 Interstitial Mn^{2+}-Driven high-aspect-ratio grain growth for low-trap-density microcrystalline films for record efficiency $CsPbI_2Br$ solar cells *ACS Energy Lett.* **3** 970–8
[26] Huang Y, Li L, Liu Z, Jiao H, He Y, Wang X, Zhu R, Wang D, Sun J and Chen Q 2017 The intrinsic properties of $FA_{(1-x)}MA_xPbI_3$ perovskite single crystals *J. Mater. Chem.* A **5** 8537–44
[27] Chen B-X, Li W-G, Rao H-S, Xu Y-F, Kuang D-B and Su C-Y 2017 Large-grained perovskite films via $FA_xMA_{1-x}Pb(IxBr_{1-x})_3$ single crystal precursor for efficient solar cells *Nano Energy* **34** 264–70
[28] Saliba M, Matsui T, Domanski K, Seo J-Y, Ummadisingu A, Zakeeruddin S M, Correa-Baena J-P, Tress W R, Abate A and Hagfeldt A 2016 Incorporation of rubidium cations into perovskite solar cells improves photovoltaic performance *Science* **354** 206–9
[29] Ding J *et al* 2019 Cesium decreases defect density and enhances optoelectronic properties of mixed $MA_{1-x}Cs_xPbBr_3$ single crystal *J. Phys. Chem.* C **123** 14969–75
[30] Du S, Jing L, Cheng X, Yuan Y, Ding J, Zhou T, Zhan X and Cui H 2018 Incorporation of cesium ions into $MA_{1-x}Cs_xPbI_3$ single crystals: crystal growth, enhancement of stability, and optoelectronic properties *J. Phys. Chem. Lett.* **9** 5833–9
[31] Philippe B, Park B-W, Lindblad R, Oscarsson J, Ahmadi S, Johansson E M J and Rensmo H 2015 Chemical and electronic structure characterization of lead halide perovskites and stability behavior under different exposures—a photoelectron spectroscopy investigation *Chem. Mater.* **27** 1720–31
[32] Li Z, Yang M, Park J-S, Wei S-H, Berry J J and Zhu K 2016 Stabilizing perovskite structures by tuning tolerance factor: formation of formamidinium and cesium lead iodide solid-state alloys *Chem. Mater.* **28** 284–92
[33] Li L, Su M, Qiu X, Zhao X, Zhu X, Wei W, Huang L, Li G, Wang Y and Sun W H 2022 Lattice relaxation effect in $Cs_xMA_{(1-x)}PbBr_3$ single crystal to enhance optoelectronic performance of perovskite photodetectors *Ceram. Int.* **48** 436–45
[34] Wang C, Zhang Y, Wang A, Wang Q, Tang H, Shen W, Li Z and Deng Z 2017 Controlled synthesis of composition tunable formamidinium cesium double cation lead halide perovskite nanowires and nanosheets with improved stability *Chem. Mater.* **29** 2157–66
[35] Dong Q, Fang Y, Shao Y, Mulligan P, Qiu J, Cao L and Huang J 2015 Electron-hole diffusion lengths$>$ 175 μm in solution-grown $CH_3NH_3PbI_3$ single crystals *Science* **347** 967–70
[36] Gao L *et al* 2016 Passivated single-crystalline $CH_3NH_3PbI_3$ nanowire photodetector with high detectivity and polarization sensitivity *Nano Lett.* **16** 7446–54
[37] Fang H and Hu W 2017 Photogating in low dimensional photodetectors *Adv. Sci.* **4** 1700323